Strategies for three-dimensional particle tracking with holographic video microscopy

3 authors, including:

Fook Chiong Cheong
Spheryx, Inc.
57 PUBLICATIONS **1,593** CITATIONS

SEE PROFILE

David G Grier
New York University
256 PUBLICATIONS **15,384** CITATIONS

SEE PROFILE

Some of the authors of this publication are also working on these related projects:

Project Active Matter View project

Project Holographic optical trapping View project

Strategies for three-dimensional particle tracking with holographic video microscopy

Fook Chiong Cheong, Bhaskar Jyoti Krishnatreya, and David G. Grier

Department of Physics and Center for Soft Matter Research, New York University, New York, NY 10003

Abstract: The video stream captured by an in-line holographic microscope can be analyzed on a frame-by-frame basis to track individual colloidal particles' three-dimensional motions with nanometer resolution. In this work, we compare the performance of two complementary analysis techniques, one based on fitting to the exact Lorenz-Mie theory and the other based on phenomenological interpretation of the scattered light field reconstructed with Rayleigh-Sommerfeld back-propagation. Although Lorenz-Mie tracking provides more information and is inherently more precise, Rayleigh-Sommerfeld reconstruction is faster and more general. The two techniques agree quantitatively on colloidal spheres' in-plane positions. Their systematic differences in axial tracking can be explained in terms of the illuminated objects' light scattering properties.

References and links

1. J. C. Crocker and D. G. Grier, "Methods of digital video microscopy for colloidal studies," J. Colloid Interface Sci. **179**, 298–310 (1996).
2. J. C. Crocker and D. G. Grier, "Microscopic measurement of the pair interaction potential of charge-stabilized colloid," Phys. Rev. Lett. **73**, 352–355 (1994).
3. G. M. Wang, E. M. Sevick, E. Mittag, D. J. Searles, and D. J. Evans, "Experimental demonstration of violations of the second law of thermodynmaics for small systems and short time scales," Phys. Rev. Lett. **89**, 050601 (2002).
4. T. G. Mason, K. Ganesan, J. H. van Zanten, D. Wirtz, and S. C. Kuo, "Particle tracking microrheology of complex fluids," Phys. Rev. Lett. **79**, 3282–3285 (1997).
5. T. T. Perkins, D. E. Smith, R. G. Larson, and S. Chu, "Stretching of a single tethered polymer in a uniform flow," Science **268**, 83–87 (1995).
6. C. Gosse and V. Croquette, "Magnetic tweezers: Micromanipulation and force measurement at the molecular level," Biophys. J. **82**, 3314–3329 (2002).
7. J. Sheng, E. Malkiel, and J. Katz, "Digital holographic microscope for measuring three-dimensional particle distributions and motions," Appl. Opt. **45**, 3893–3901 (2006).
8. S.-H. Lee and D. G. Grier, "Holographic microscopy of holographically trapped three-dimensional structures," Opt. Express **15**, 1505–1512 (2007).
9. S.-H. Lee, Y. Roichman, G.-R. Yi, S.-H. Kim, S.-M. Yang, A. van Blaaderen, P. van Oostrum, and D. G. Grier, "Characterizing and tracking single colloidal particles with video holographic microscopy," Opt. Express **15**, 18,275–18,282 (2007).
10. F. C. Cheong, B. Sun, R. Dreyfus, Amato-Grill, K. Xiao, L. Dixon, and D. G. Grier, "Flow visualization and flow cytometry with holographic video microscopy," Opt. Express **17**, 13,071–13,079 (2009).
11. F. C. Cheong, K. Xiao, and D. G. Grier, "Characterization of individual milk fat globules with holographic video microscopy," J. Dairy Sci. **92**, 95–99 (2009).
12. J. W. Goodman, *Introduction to Fourier Optics*, 3rd ed. (McGraw-Hill, New York, 2005).

13. J. Garcia-Sucerquia, W. Xu, S. K. Jericho, P. Klages, M. H. Jericho, and H. J. Kreuzer, "Digital in-line holographic microscopy," Appl. Opt. **45**, 836–850 (2006).
14. F. C. Cheong and D. G. Grier, "Rotational and translational diffusion of copper oxide nanorods measured with holographic video microscopy," Opt. Express **18**, 6555–6562 (2010).
15. F. Dubois, L. Joannes, and J. C. Legros, "Improved three-dimensional imaging with a digital holography microscope with a source of partial spatial coherence," Appl. Opt. **38**, 7085–7094 (1999).
16. J. Garcia-Sucerquia, J. H. Ramírez, and R. Castaneda, "Incoherent recovering of the spatial resolution in digital holography," Opt. Commun. **260**, 62–67 (2006).
17. C. F. Bohren and D. R. Huffman, *Absorption and Scattering of Light by Small Particles* (Wiley Interscience, New York, 1983).
18. M. I. Mishchenko, L. D. Travis, and A. A. Lacis, *Scattering, Absorption and Emission of Light by Small Particles* (Cambridge University Press, Cambridge, 2001).
19. W. J. Lentz, "Generating Bessel functions in Mie scattering calculations using continued fractions," Appl. Opt. **15**, 668–671 (1976).
20. W. J. Wiscombe, "Improved Mie scattering algorithms," Appl. Opt. **19**, 1505–1509 (1980).
21. C. B. Markwardt, "Non-linear least squares fitting in IDL with MPFIT," in *Astronomical Data Analysis Software and Systems XVIII*, D. Bohlender, P. Dowler, and D. Durand, eds. (Astronomical Society of the Pacific, San Francisco, 2009).
22. J. Moré, "The Levenberg-Marquardt algorithm: Implementation and theory," in *Numerical Analysis*, G. A. Watson, ed., vol. 630, p. 105 (Springer-Verlag, Berlin, 1977).
23. B. Rappaz, P. Marquet, E. Cuche, Y. Emery, C. Depeursinge, and P. J. Magistretti, "Measurement of the integral refractive index and dynamic cell morphometry of living cells with digital holographic microscopy," Opt. Express **13**, 9361–9373 (2005).
24. G. C. Sherman, "Application of the convolution theorem to Rayleigh's integral formulas," J. Opt. Soc. Am. **57**, 546–547 (1967).
25. U. Schnars and W. P. O. Jüptner, "Digital recording and reconstruction of holograms," Meas. Sci. Tech. **13**, R85–R101 (2002).
26. E. R. Dufresne and D. G. Grier, "Optical tweezer arrays and optical substrates created with diffractive optical elements," Rev. Sci. Instrum. **69**, 1974–1977 (1998).
27. D. G. Grier, "A revolution in optical manipulation," Nature **424**, 810–816 (2003).
28. M. Polin, K. Ladavac, S.-H. Lee, Y. Roichman, and D. G. Grier, "Optimized holographic optical traps," Opt. Express **13**(15), 5831–5845 (2005).
29. P. Messmer, P. J. Mullowney, and B. E. Granger, "GPULib: GPU computing in high-level languages," Comp. Sci. Engin. **10**, 70–73 (2008).
30. K. Xiao and D. G. Grier, "Multidimensional optical fractionation with holographic verification," Phys. Rev. Lett. **104**, 028302 (2010).
31. F. C. Cheong, S. Duarte, S.-H. Lee, and D. G. Grier, "Holographic microrheology of polysaccharides from *Streptococcus mutans* biofilms," Rheol. Acta **48**, 109–115 (2009).

1. Introduction

Particle tracking based on quantitative analysis of video microscopy images [1] has become a standard technique in several branches of science and engineering. Time-resolved particle trajectories obtained from sequences of video images have been used to study the interactions between colloidal particles [2], to address fundamental questions in statistical physics [3], to probe the viscoelastic properties of soft media [4] and to measure the dynamical properties of single polymers [5], among many other applications. Most of these studies have focused on motion parallel to the microscope's focal plane because three-dimensional tracking with conventional techniques requires extensive calibrations and accesses only a limited axial range [6]. Recent advances in in-line holographic video microscopy [7, 8, 9, 10] promise to overcome these limitations, providing access to three-dimensional trajectory data with nanometer resolution over very large volumes, with only the overall magnification of the optical train requiring calibration.

Here, we report on a head-to-head comparison between two complementary approaches to analyzing holographic video snapshots. The first involves fitting each image to predictions of the Lorenz-Mie theory of light scattering [9, 10]. It provides a wealth of information with outstanding resolution [9, 10, 11], but is computationally very demanding and works only for

particles whose light-scattering properties are described well by the theory. The second is more general and less computationally expensive, but relies on phenomenological interpretation to yield particle-tracking information. This approach uses Fourier diffraction theory [12] to approximately reconstruct the three-dimensional light field responsible for the recorded hologram [7, 8, 13] and associates features in this reconstruction with the structure [14] and orientation [7, 8, 14] of the sample. Using measurements on micrometer-scale colloidal spheres as a test case, we demonstrate that these two approaches agree quantitatively, except for a systematic offset in the measured axial positions, which can be accounted for quantitatively with Lorenz-Mie optics.

2. In-line Holographic Video Microscopy

Our in-line holographic microscope, depicted schematically in Fig. 1(a), is based on a commercial inverted light microscope (Nikon TE 2000U). The collimated beam from a 10 mW He-Ne laser (Uniphase, $\lambda = 632.8$ nm) replaces the conventional incandescent illuminator. The resulting irradiance of roughly 10 nW/μm^2 is comparable to that of conventional microscope illumination and is too weak to exert measurable forces on the illuminated objects or to heat the sample appreciably. An object at position $\mathbf{r}_p$ scatters a small portion of the incident plane wave, as depicted in Fig. 1. The scattered light then propagates to the focal plane of the microscope, where it interferes with the unscattered portion of the laser beam. The resulting interference pattern is magnified by the microscope's objective lens (Nikon Plan Apo, 100×, numerical aperture 1.4, oil immersion) and projected by a video eyepiece (0.63×) onto a CCD camera (NEC TI-324AII), which records its intensity at 30 frames/s with an exposure time of 1 ms. The resulting video signal is recorded as uncompressed digital video with a digital video recorder (Pioneer DVR-520H) before being analyzed.

This system provides a calibrated magnification of 0.135 μm/pixel. When used with conventional illumination and analyzed with standard methods of digital video microscopy [1], it typically yields a micrometer-scale sphere's in-plane position to within 1/10 pixel, or roughly 10 nm. With appropriate calibration, a sphere's axial position also can be measured to within 100 nm [1]. The axial range, however, is restricted to roughly ± 5 μm by the limited depth of focus of the high-numerical-aperture objective lens. Illuminating the sample instead with coherent light provides access to more information at much higher resolution and over a much larger axial range, without requiring detailed calibrations. Extracting this information, however, requires a substantially more sophisticated analysis strategy.
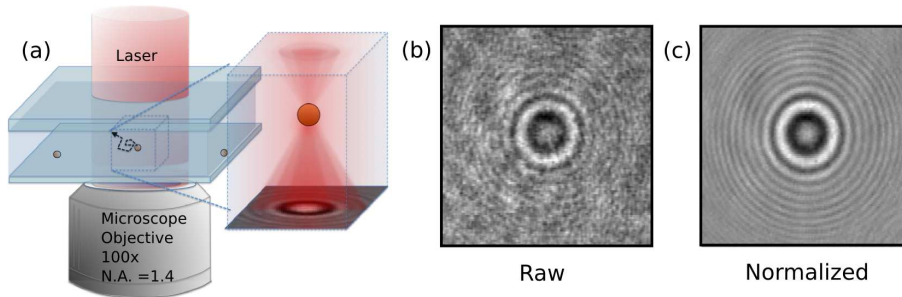

Fig. 1. (a) In-line holographic video microscope. A collimated laser beam illuminates the sample. Light scattered by the sample interferes with the unscattered portion of the beam in the focal plane of the objective lens. The interference pattern is magnified, recorded and then analyzed to obtain measurements of the particle's position. (b) Unprocessed hologram recorded by the video camera. (c) The corresponding normalized hologram.

The unprocessed holographic image of a colloidal sphere in Fig. 1(b) illustrates some of the challenges of in-line holographic microscopy. In addition to the sphere's light-scattering pattern, this image is marred by speckle and is obscured by fringes due to all of the other surfaces and particles along the optical train. Many of these distracting features could be mitigated by reducing the correlation length of the illumination [15], for example with a rotating diffuser [16]. This, however, would reduce the benefits of holographic imaging relative to conventional incoherent imaging. Most of the unwanted interference fringes could be scaled out of the spatial bandwidth of the imaging system by illuminating the sample with a diverging laser beam. Collimated illumination, however, presents a much simpler scattering geometry that lends itself to precision analysis.

3. Holographic Particle Tracking

We model the incident illumination as a plane wave,

$$\mathbf{E}_0(\mathbf{r}, z) = u_0(\mathbf{r}) e^{ikz} \hat{\varepsilon}_0, \tag{1}$$

propagating along $\hat{z}$ with wavenumber $k = 2\pi n_m/\lambda$ in a medium of refractive index n_m. Both the transverse amplitude profile $u_0(\mathbf{r})$ and the polarization $\hat{\varepsilon}_0$ are assumed to be independent of z. The wave scattered by the sample,

$$\mathbf{E}_s(\mathbf{r}, z) = E_s(\mathbf{r}, z) \hat{\varepsilon}(\mathbf{r}, z) \tag{2}$$

propagates in three dimensions with complex amplitude $E_s(\mathbf{r}, z)$ and spatially varying polarization $\hat{\varepsilon}(\mathbf{r}, z)$. The measured intensity at point $\mathbf{r}$ in the focal plane is due to the superposition of the incident and scattered waves,

$$I(\mathbf{r}) = |\mathbf{E}_0(\mathbf{r}, 0) + \mathbf{E}_S(\mathbf{r}, 0)|^2 \tag{3}$$

$$= u_0^2(\mathbf{r}) + 2\Re\left\{u_0(\mathbf{r}) E_s(\mathbf{r}, 0) \hat{\varepsilon}_0^* \cdot \hat{\varepsilon}(\mathbf{r}, 0)\right\} + |E_s(\mathbf{r}, 0)|^2. \tag{4}$$

If we assume that most of the static defects in the recorded image arise from variation in the illumination, then they can be removed by normalizing $I(\mathbf{r})$ with a measured background image [8, 10, 11, 14]. The success of this procedure can be judged by the normalized hologram in Fig. 1(c), whose visual quality approaches that of a conventional microscope image. Assuming, furthermore, that the object's height above the focal plane is greater than its size, the geometric rotation of the scattered polarization will be comparatively small, so that $\hat{\varepsilon}_0^* \cdot \hat{\varepsilon}(\mathbf{r}, 0) \approx 1$. This approximation can be improved by deliberately defocusing the microscope. An optically isotropic sample's normalized hologram then is described by

$$b(\mathbf{r}) \approx 1 + 2\Re\left\{E_R(\mathbf{r}, 0)\right\} + |E_R(\mathbf{r}, 0)|^2, \tag{5}$$

where the reduced scattered field is $E_R(\mathbf{r}, z) = E_s(\mathbf{r}, z)/u_0(\mathbf{r})$.

Equation (5) is the point of departure for the two approaches to holographic particle tracking that we will compare. The first involves fitting the recorded images to predictions of the exact Lorenz-Mie theory for light scattering. The second involves tracking features in the three-dimensional light field reconstructed from a recorded hologram using the Rayleigh-Sommerfeld diffraction integral.

3.1. Lorenz-Mie Fitting

The scattered field at position $\mathbf{r}$ in the focal plane due to an object at $\mathbf{r}_p$ relative to the center of the focal plane may be written as

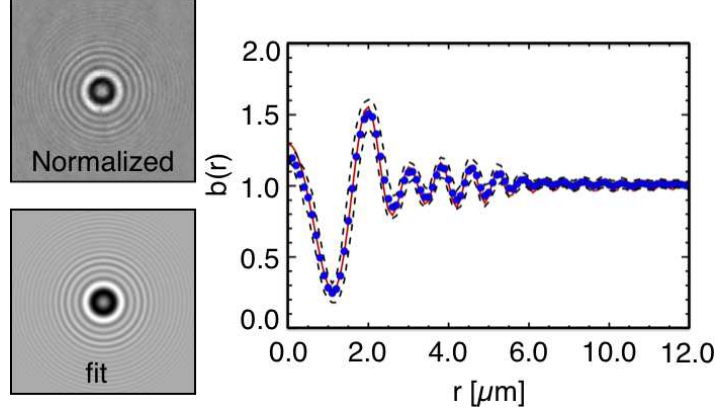$$\mathbf{E}_s(\mathbf{r}, 0) = u_0(\mathbf{r}_p) \mathbf{f}_s(k(\mathbf{r} - \mathbf{r}_p)), \tag{6}$$

Fig. 2. Lorenz-Mie particle tracking and characterization. The upper image is the normalized hologram $b(\mathbf{r})$ of a 1.51 μm diameter polystyrene sphere in water. The lower image is a fit to the Lorenz-Mie theory. The solid curve is the azimuthal average $b(r)$ of the measured intensity around the center identified by the fit. Dashed curves indicate the azimuthal standard deviation of the hologram's values, and indicates the measurement error. Plot points show the corresponding radial profiles of the fit. Error bars on the fit values are smaller than the plot symbols.

where $\mathbf{f}_s(\mathbf{r})$ is the normalized scattering function. In this case, Eq. (5) reduces to

$$b(\mathbf{r}) = 1 + 2\Re\left\{\mathbf{f}_s(k(\mathbf{r} - \mathbf{r}_p)) \cdot \hat{\varepsilon}_0\right\} + \left|\mathbf{f}_s(k(\mathbf{r} - \mathbf{r}_p))\right|^2. \tag{7}$$

Given an analytic form for $\mathbf{f}_s(k\mathbf{r})$, a normalized hologram may be fit to Eq. (7) for the position of the particle $\mathbf{r}_p$ as well as any free parameters in the scattering function [9].

Lorenz-Mie theory describes the scattering function as an expansion [17]

$$\mathbf{f}_s(k\mathbf{r}) = \sum_{n=1}^{n_c} \frac{i^n(2n+1)}{n(n+1)}\left(i\,\alpha_n\mathbf{N}_{e1n}^{(3)}(k\mathbf{r}) - \beta_n\mathbf{M}_{o1n}^{(3)}(k\mathbf{r})\right) \tag{8}$$

in the vector spherical harmonics, $\mathbf{N}_{e1n}^{(3)}(k\mathbf{r})$ and $\mathbf{M}_{o1n}^{(3)}(k\mathbf{r})$, whose coefficients, α_n and β_n, depend on the size, shape, composition, and orientation of the object and on the structure of the illuminating field. For a homogeneous isotropic sphere of radius a_p and refractive index n_p illuminated by a linearly polarized plane wave, the expansion coefficients are expressed in terms of spherical Bessel functions and spherical Hankel functions as [17]

$$\alpha_n = \frac{m^2 j_n(mka_p)\,[ka_p\,j_n(ka_p)]' - j_n(ka_p)\,[mka_p\,j_n(mka_p)]'}{m^2 j_n(mka_p)\,[ka_p\,h_n^{(1)}(ka_p)]' - h_n^{(1)}(ka_p)\,[mka_p\,j_n(mka_p)]'} \quad \text{and} \tag{9}$$

$$\beta_n = \frac{j_n(mka_p)\,[ka_p\,j_n(ka_p)]' - j_n(ka_p)\,[mka_p\,j_n(mka_p)]'}{j_n(mka_p)\,[ka_p\,h_n^{(1)}(ka_p)]' - h_n^{(1)}(ka_p)\,[mka_p\,j_n(mka_p)]'}, \tag{10}$$

where $m = n_p/n_m$ and where primes denote derivatives with respect to the argument. This form assumes $\hat{\varepsilon}_0 = \hat{x}$, which is appropriate for our microscope. The scattering coefficients fall off rapidly with order n, and the series is found to converge after a number of terms $n_c = ka_p + 4.05\,(ka_p)^{1/3} + 2$ [17, 18], which typically is less than 30 for micrometer-scale latex spheres in water. To compute $\mathbf{f}_s(k\mathbf{r})$ in practice, we use the accurate but numerically intensive continued fraction algorithm due to Lentz for the expansion coefficients [19] and the more efficient recurrence algorithm due to Wiscombe for the vector spherical harmonics [20].

The images in Fig. 2 are the normalized image of a 1.51 μm diameter polystyrene sphere in water (Polysciences Lot 526826) and a pixel-by-pixel nonlinear least-squares fit to Eqs. (7) through (10) for $\mathbf{r}_p$, a_p and n_p. Fits are performed with the MPFIT implementation [21] of the Levenberg-Marquardt algorithm [22] whose rigorous estimates for the adjustable parameters' uncertainties suggest that the sphere's center has been identified with a precision of 1 nm in all three dimensions. This estimate of the measurement resolution has been confirmed by independent measurements of similar colloidal particles' dynamics [9, 10]. Similar part-per-thousand resolution is achieved for the particle's radius and refractive index. The quality of the fit can be seen in the azimuthally averaged results that also are plotted in Fig. 2. In this particular example, the particle is found to have a radius of $a_p = 0.816 \pm 0.001$ μm, a purely real refractive index of $n_p = 1.5821 \pm 0.0006$, and is centered at $z_p = 11.534 \pm 0.003$ μm above the focal plane.

Fits to Lorenz-Mie theory can be this successful because the interference fringes in each holographic image can be defocused enough to cover thousands of pixels. In conventional bright-field imaging, by contrast, a particle at such a large height above the focal plane would be effectively invisible.

If the illumination were not sufficiently collimated, the incident wavefronts' curvature would introduce position-dependent distortions into the holograms that would not be accounted for by Eq. (7). We find the fit values for a particle's size and refractive index to be independent of its position in the microscope's 78×65 μm^2 field of view. Wavefront curvature therefore should not affect estimates for particles' positions.

3.2. Rayleigh-Sommerfeld Back-Propagation

The hologram of a colloidal particle also can be used to reconstruct the three-dimensional light field that created the hologram. Although such reconstructions may be treated as volumetric renderings of the scattered object [7, 8, 23], they are more properly interpreted as renderings of the scattered field, $\mathbf{E}_s(\mathbf{r},z)$ or its intensity, $|E_s(\mathbf{r},z)|^2$. Such volumetric reconstructions can
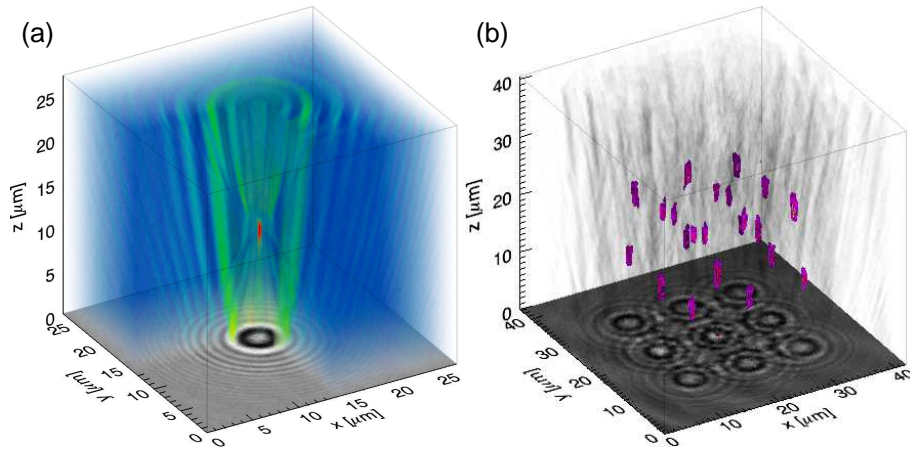

Fig. 3. Rayleigh-Sommerfeld back-propagation. (a) Volumetric reconstruction of the scattered intensity due to a single colloidal sphere, colored by intensity. The diverging rays arise from the spurious mirror image of the sphere in the focal plane. (b) Volumetric reconstructions of 22 individual 1.58 μm diameter silica spheres organized in body center crystalline lattice with holographic optical tweezers in distilled water. Colored regions indicate the isosurface of the brightest 1 percent of reconstructed voxels. (Media 1)

be computed from any hologram without knowledge of the scattering object's shape, size or composition. They also are much less computationally expensive than Lorenz-Mie fits. Features in the reconstructed light field may be associated with the positions and orientations of objects in the scattering volume [7, 8, 14]. Volumetric reconstructions therefore promise high-speed model-free measurements of multiple objects' positions and motions in three dimensions. How objects' actual positions are related to features in their back-projected holograms has not been assessed quantitatively in previous studies, however. To address this, we compare the precision measurements of the previous section with three-dimensional particle tracking results obtained with Rayleigh-Sommerfeld back propagation.

The wave scattered by a particle spreads as it propagates. Its amplitude, consequently, should be substantially smaller than the illumination's once it reaches the focal plane. In that case, the third term in Eq. (5) is negligible compared with the other two and

$$b(\mathbf{r}) - 1 \approx 2\Re\{E_R(\mathbf{r}, 0)\}. \tag{11}$$

If the complex scattered field were completely specified in the focal plane, it could be reconstructed at height z above the focal plane as the convolution,

$$E_s(\mathbf{r}, z) = E_s(\mathbf{r}, 0) \otimes h_{-z}(\mathbf{r}) \tag{12}$$

of the scattered amplitude in the focal plane with the Rayleigh-Sommerfeld propagator [12]

$$h_{-z}(\mathbf{r}) = \frac{1}{2\pi} \frac{\partial}{\partial z} \frac{e^{ikR}}{R}, \tag{13}$$

where $R^2 = r^2 + z^2$. The sign convention for z accounts for the object's position upstream of the focal plane. Equation (12) may be rewritten with the Fourier convolution theorem as

$$U(\mathbf{q}, z) = U(\mathbf{q}, 0) H(\mathbf{q}, -z), \tag{14}$$

where

$$U(\mathbf{q}, z) = \int_{-\infty}^{\infty} E_s(\mathbf{r}, z) e^{-i\mathbf{q} \cdot \mathbf{r}} d^2 r \tag{15}$$

and [24, 25, 12]

$$H(\mathbf{q}, -z) = e^{iz(k^2 - q^2)^{\frac{1}{2}}}. \tag{16}$$

To use this formalism to reconstruct the scattered field, we note that the Fourier transform of $b(\mathbf{r}) - 1$ is

$$B(\mathbf{q}) \approx U_R(\mathbf{q}, 0) + U_R^*(\mathbf{q}, 0), \tag{17}$$

where $U_R(\mathbf{q}, z)$ is the Fourier transform of $E_R(\mathbf{r}, z)$. From this,

$$B(\mathbf{q}) H(\mathbf{q}, -z) = U_R(\mathbf{q}, z) + U_R^*(\mathbf{q}, -z) \tag{18}$$

may be recognized to be the superposition of the scattered field at height z above the focal plane and a spurious field due to the object's mirror image in the focal plane, which is known as the twin image. The twin image's influence on the reconstructed field is reduced by defocusing, which also improves the approximations underlying Eq. (11). In the further approximation that the illumination is uniform, the reconstructed scattered field is

$$E_s(\mathbf{r}, z) \approx \frac{e^{-ikz}}{4\pi^2} \int_{-\infty}^{\infty} B(\mathbf{q}) H(\mathbf{q}, -z) e^{i\mathbf{q} \cdot \mathbf{r}} d^2 q. \tag{19}$$

The associated intensity, $I_s(\mathbf{r},z) = |E_s(\mathbf{r},z)|^2$, is an estimate for the scattered light's intensity at height z above the focal plane. The example in Fig. 3(a) shows a typical volumetric reconstruction in 0.135 μm slices for a 1.5 μm diameter polystyrene sphere in water, the reconstructed rays converging to the diffraction-limited bright red spot roughly 10 μm above the focal plane.

Because the projection operation in Eq. (12) assumes the medium to be homogeneous and isotropic, it cannot account for light's distortion by the object itself. Consequently, the reconstructed field upstream of an object is degraded by artifacts, as is the case for $z > 12$ μm in Fig. 3(a). Reconstruction artifacts overlap the images of objects that are located upstream of a scattering particle. Nevertheless, the volumetric image in Fig. 3(b) (Media 1) of the intensity scattered by a collection 1.58 μm diameter silica spheres in water (Duke Scientific Lot 24169) shows clearly resolved maxima, even when spheres are occluded by their neighbors [8]. These 22 spheres were arranged with holographic optical traps [26, 27, 28] into a body-centered cubic (bcc) lattice with a 10.8 μm lattice constant. The colored regions in Fig. 3(b) (Media 1) are isosurfaces of the brightest 1 percent of the reconstructed voxels and clearly suggest the positions of all of the spheres in the lattice. Interpreting such a complicated hologram with fits to Lorenz-Mie theory would be challenging.
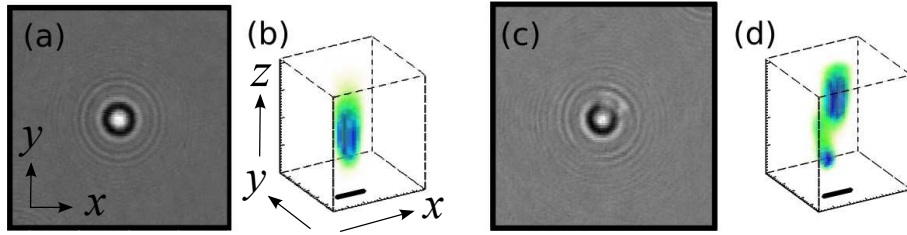

Fig. 4. Rayleigh-Sommerfeld back-propagation of aspherical objects. (a) Hologram of a colloidal silica sphere in water. (b) Detail of the brightest region of the volumetric reconstruction showing a symmetric structure. (c) Hologram of a silica sphere that is partially coated with 40 nm of permalloy. (d) Volumetric reconstruction showing asymmetric structure. Scale bars in (b) and (d) indicate 1 μm.

Whereas Lorenz-Mie fitting requires a specific model for each object's light scattering properties, Rayleigh-Sommerfeld back-propagation also can be applied to objects whose structures are not known, or for which no numerically stable scattering function is available. To illustrate this, the normalized holograms in Figures 4(a) and (c) were obtained with two 1.58 μm diameter silica spheres, the second of which had a 40 nm thick cap of permalloy (80% Ni and 20% Fe) applied to roughly on octant. Asymmetric structure in the latter particle's hologram arises from the the superposition of two contributions, the symmetric scattering pattern due to the sphere and another less well characterized contribution from its cap. Asymmetries in the hologram change form and direction as the capped sphere rotates. This structure also is apparent in the volumetric reconstructions in Figs. 4(b) and (c). Whereas the uncapped sphere gives rise to a rotationally symmetric intensity pattern, the capped sphere's volumetric image has obvious structure. Both the location of the capped sphere and an indication of its orientation are captured by the volumetric reconstruction in Figure 4, whose intensity maximum contrasts with those of ordinary spheres in that it is asymmetric.

It is tempting to associate the positions [1] of local maxima in the reconstructed intensity distribution with the actual positions of objects in the sample [7, 8]. The approximations used in deriving Eq. (19) coupled with the nonlinear phenomenological centroid identification [1] make it difficult to assess this method's accuracy and resolution *a priori*. Comparison with results of Lorenz-Mie analysis addresses this need.
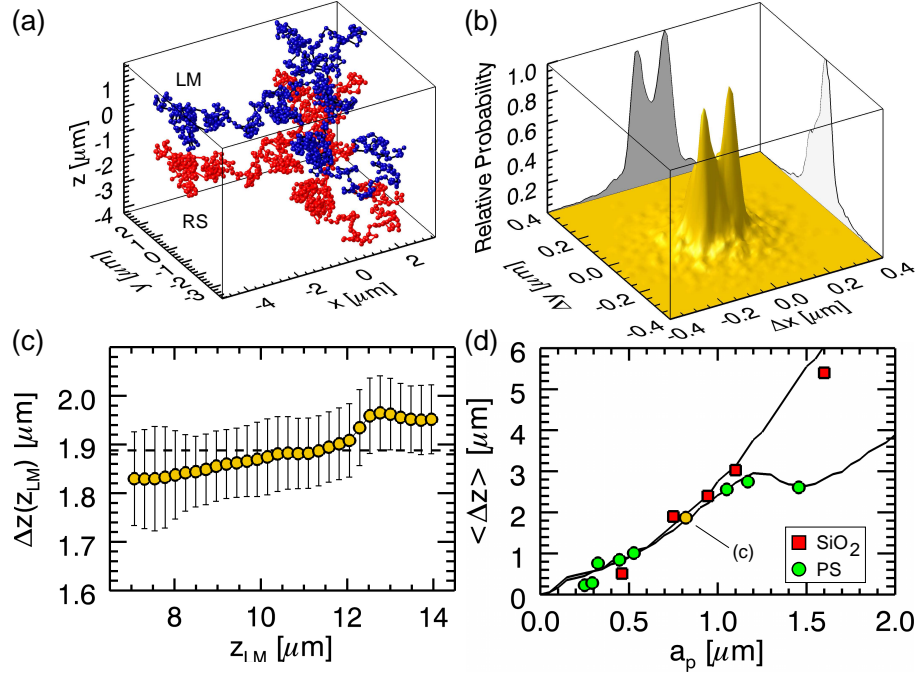
4. Comparison of Strategies

Fig. 5. Comparison of Lorenz-Mie and Rayleigh-Sommerfeld particle-tracking algorithms. (a) Trajectory of a colloidal silica sphere at 1/30 s intervals obtained with the two strategies. Each point indicates the position of the sphere in one holographic snapshot as estimated by the Lorenz-Mie (LM) and Rayleigh-Sommerfeld (RS) approaches. (b) Distribution of differences Δx and Δy in the in-plane position estimated by the two strategies. (c) Mean difference $\Delta z(z_{LM})$ in the axial position as a function of the Lorenz-Mie estimate z_{LM}, obtained from 10,000 measurements. (d) Mean difference $\langle \Delta z(a_p) \rangle$ in axial position as a function of sphere radius a_p for polystyrene (PS) spheres (circles) and silica (SiO$_2$) spheres (squares). Solid curves are predictions of Lorenz-Mie theory.

Figure 5(a) shows 10 s in the 10 min duration trajectory of a 1.5 μm diameter polystyrene sphere diffusing in water sampled at 1/30 s and analyzed with both Lorenz-Mie fitting and Rayleigh-Sommerfeld back-propagation. The two approaches agree quantitatively on the particle's in-plane position, as is shown by the histogram of differences in Fig. 5(b). This distribution has peaks at 0.35 pixel offsets because brightness-weighted centroid detection is biased toward pixels' centers unless particular care is taken to match the detection window to the size of the object [1]. Because the resolution of the Lorenz-Mie fits is consistently better than 1 nm over the entire trajectory, the difference can be ascribed entirely to errors in interpreting the Rayleigh-Sommerfeld reconstructions.

Figure 5(c) shows the distribution of differences $\Delta z(z_{LM}) = z_{RS} - z_{LM}$ of axial positions measured with Rayleigh-Sommerfeld (RS) back propagation and Lorenz-Mie (LM) fitting as a function of z_{LM}. These differences are normally distributed about $\langle \Delta z \rangle = 1.89$ μm and vary only slightly with axial position.

This systematic offset can be ascribed to the fundamental difference in what the two methods track. The Lorenz-Mie approach uses the exact theory for light scattering by a sphere. It therefore yields an estimate for the actual three-dimensional position of the sphere's center relative to

the center of the focal plane. The Rayleigh-Sommerfeld approach, by contrast, seeks the center of brightness in the reconstructed scattering pattern, which generally falls downstream of the sample's center. This distinction has been noted in passing by previous studies [7, 8]. How it varies with the sample's position and physical properties has not previously been addressed.

Although the axial offset plotted in Fig. 5(c) varies only weakly with axial position, the data in Fig. 5(d) for colloidal silica and polystyrene spheres of varying radii show a much stronger dependence on both composition and size. This means that back-propagation cannot reliably be used to measure three-dimensional separations in polydisperse and heterogeneous samples. Lorenz-Mie analysis accounts explicitly for individual spheres' size and refractive index and so should provide accurate estimates for axial positions regardless of size and composition.

Trends in the observed axial offsets constitute a self-consistency test both for the analyses and also for our instrumentation. The solid curves in Fig. 5 represent the distance from the center of a sphere to the point of maximum intensity in its forward scattering pattern computed with Eqs. (8) through (10). This distance should correspond to the difference in axial position obtained with Rayleigh-Sommerfeld and Lorenz-Mie analyses. Quantitative agreement between these predictions and our measurements on two different materials over an order of magnitude in particle size supports both the correctness of our analysis and also the efficacy of our experimental implementation.

The axial offset is comparable to the measurement error in the Rayleigh-Sommerfeld method for the smallest spheres in Fig. 5(d). This observation suggests that objects with features smaller than the wavelength of light may be tracked in three dimensions at high resolution using Rayleigh-Sommerfeld back propagation, even if the shape and composition of the object is not known. This, in turn, explains why Rayleigh-Sommerfeld back-propagation has proved successful at tracking the three-dimensional positions and orientations of diffusing metal oxide nanorods, two of whose dimensions are smaller than the wavelength of light [14].

Although Rayleigh-Sommerfeld back-propagation provides less information than Lorenz-Mie fitting, it is more flexible and substantially faster. Computing each reconstructed axial slice requires roughly a dozen float-point array operations and a Fourier transform. Depending on the desired axial range and resolution, a few hundred slices may be computed for a single volume. By contrast, each evaluation of the Lorenz-Mie scattering function with Eq. (8) requires well over a hundred float-point array operations, and each fit requires as many as a hundred evaluations. Ten full Rayleigh-Sommerfeld reconstructions consequently can be computed in the time required for a single Lorenz-Mie fit. Identifying and locating maxima in the reconstructions does not add substantially to the processing time [1].

We reduce the computational overhead of both analysis methods by performing array calculations on the graphical processing unit (GPU) of a high-end graphics card using the GPUlib library [10, 29]. Hardware-accelerated analysis typically yields ten volumetric reconstructions per second or one Lorenz-Mie fit, which is fast enough for near-real-time characterization of individual colloidal particles [9, 10, 11, 30], visualization of three-dimensional flows [10], measurement of rheological properties [31] and performance of medical diagnostic tests [10].

5. Conclusion

Our measurements on colloidal spheres demonstrate that Rayleigh-Sommerfeld back-propagation can be a fast, flexible and effective method for tracking objects in three dimensions. Axial positions obtained by tracking intensity maxima in the reconstructed light field differ systematically from the true position for spheres larger than the wavelength of light. These deviations depend on the spheres' size and refractive index, and thus can lead to errors in estimates for relative separations among dissimilar objects in three dimensions. Fortunately, particles smaller than the wavelength of light have negligibly small offsets, suggesting that

Rayleigh-Sommerfeld back propagation may be most useful for analyzing the motions of small objects whose shapes sizes and compositions are unknown.

Our comparison of these techniques over an order of magnitude in particle size suggests that the measurement error in Rayleigh-Sommerfeld tracking can be better than 100 nm in all directions over the entire accessible axial range. Although this compares poorly with the nanometer resolution of Lorenz-Mie tracking, Rayleigh-Sommerfeld tracking appears to be more effective for many-body systems and can be applied to objects of any shape [14].

Alternatives to Lorenz-Mie theory such as the discrete dipole approximation (DDA) or finite difference time-domain (FDTD) calculations may be able to provide the basis for high-resolution tracking and characterization for more highly structured samples than isotropic homogeneous spheres. In all such cases, Rayleigh-Sommerfeld back-propagation can provide a useful starting point for the fitting process, provided that account is taken of the size- and composition-dependent axial offset.

6. Acknowledgements